DYNAMIC BUCKLING OF IMPULSIVELY LOADED PRISMATIC CORES

Enrico Ferri, Emilio Antinucci, Ming Y. He, John W. Hutchinson, Frank W. Zok and Anthony G. Evans

DYNAMIC BUCKLING OF IMPULSIVELY LOADED PRISMATIC CORES

ENRICO FERRI, EMILIO ANTINUCCI, MING Y. HE, JOHN W.
HUTCHINSON, FRANK W. ZOK AND ANTHONY G. EVANS

When sandwich panels with prismatic cores are impulsively loaded, the stresses imposed by the core on the front face, as well as those transmitted through the core govern the response metrics, especially the center displacement, resistance to tearing, and loads transmitted to the supports. This article presents a basic study of the dynamic response with emphasis on the I-core. A prior assessment revealed buck-lewaves induced because of inertial phenomena accompanying the rapid compression of the members. The development of these waves is an integral aspect of the dynamic response. One objective of this investigation is to ascertain the characteristics governing such waves in I-core configurations through a combined experimental and numerical study. A particular emphasis is on the influence of manufacturing imperfections in the core members on the formation and propagation of the buckles. A second goal is to examine the stresses associated with the dynamic compression of the core, again through a combined experimental and numerical investigation.

The investigation is conducted for stainless steel I-core panels supported at the back face and subjected to a constant velocity at the front. Imperfections to be included in the numerical study have been ascertained by comparing buckle patterns with those found experimentally over the relevant velocity range. The simulations reveal that the stresses induced differ on the front and back faces. On the front they are higher and velocity dependent. On the rear they are velocity invariant and scale with the relative density and material yield strength. The duration of the stress pulses, which is essentially the same on both faces, scales linearly with the core height. It correlates with the time needed for bucklewaves to propagate through the core to the back face. After the pulse terminates, the core continues to compress at a stress level about an order of magnitude smaller.

1. Introduction

Insights regarding the response of metallic sandwich panels to water blast have been gained by recent assessments of the fluid/structure interaction (FSI). Most crucial has been the discovery of soft and strong core responses, dependent on such factors as the dynamic strength of the core, its thickness, and the magnitude of the impulse [Liang et al. 2007]. When a soft response can be elicited through the appropriate design of the core, the performance metrics are beneficially affected. In particular, the forces transmitted to the supports, the center deflection, and the strains induced in the faces are all reduced. This happens because the time required to crush the core exceeds that needed for the plastic deformation to propagate laterally from the supports to the center of the panel. However, the soft design must assure

that the front face does not slap into the back. Otherwise the performance inverts and the metrics become adversely affected.

Fundamental mechanics guiding the selection of soft cores (while averting slapping) has been devised for cores that crush at constant dynamic strength (such as foams and multilayer truss configurations) [Fleck and Deshpande 2004; Tilbrook et al. 2006; Wei et al. 2007]. The situation differs for prismatic cores such as I-, X-, Y- and Z- cores because these do not exhibit constant dynamic crush strength [Radford et al. 2007]. The purpose of this article is to contribute to the understanding of the dynamic crushing of prismatic cores with the eventual goal of using this knowledge to distinguish between soft and strong responses.

Progress toward the objective of understanding the dynamics of core compression has been made by examining the response of slender columns to a velocity, v_0, abruptly imposed at one end [Abrahamson and Goodier 1966; Vaughn et al. 2005; Vaughn and Hutchinson 2006]. Short wavelength buckles have been shown to form (Figure 1) having wavelength that depends on v_0 as well as the slenderness of the members. These bucklewaves influence the strains that can be induced in the members, as well as the stresses transmitted into the supporting structure. Building upon the insights provided by the bucklewave analysis, a combined experimental and numerical investigation is pursued in this article.

Since transitions between soft and strong responses can be induced in I-cores [Liang et al. 2007], this geometry provides a convenient test bed to examine the concepts. In the present study, cores are fabricated from stainless steel and tested under conditions that impose a constant velocity at one end.
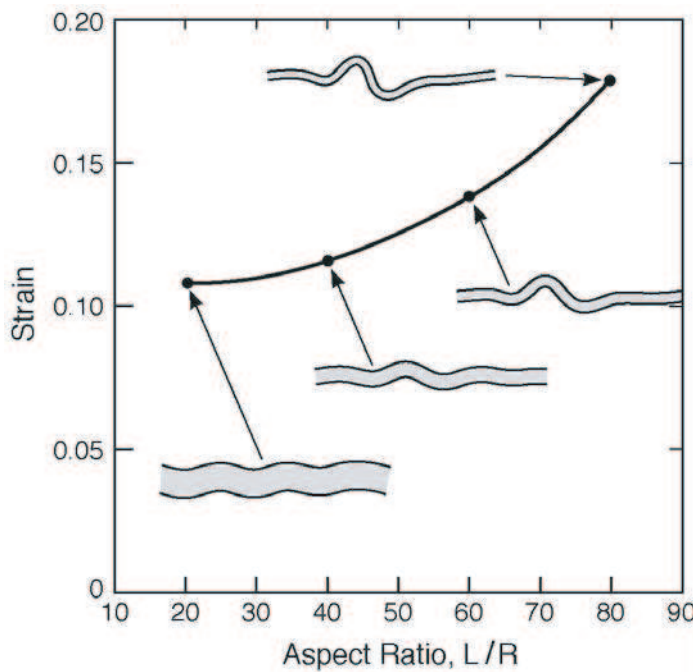

Figure 1. Buckle waves generated in free standing slender columns subject to a constant velocity at one end (the left). The plot indicates the terminal value of the nominal plastic strain [Vaughn and Hutchinson 2006].

Since the response is sensitive to the buckling modes, as well as to the wavelength and amplitude of imperfections, one focus of the experiments is on a classification of the preferred dynamic modes. For this purpose, a high speed camera is used to monitor the bucklewaves. Thereafter, the classification is used to select the modes relevant to realistic numerical simulations conducted using ABAQUS Explicit.

Ultimately, the stresses transmitted through the members are most relevant to the assessment of prismatic sandwich structures. These stresses are measured using a Hopkinson bar and the results used to validate the numerical simulations. Thereafter, simulations are used to provide basic understanding of the stress wave propagation and buckling phenomena, and of the magnitude and duration of the transmitted pressure pulse. The results provide the insight needed for analytic models.

To achieve the preceding objectives, this article is organized in the following manner. In Section 2, the experimental methods are described. In Section 3, the measurements and observations are presented. In Section 4, the dynamic modes are ascertained and the sensitivity of the simulations to imperfections is established. The buckle patterns are also determined. In Section 5, the dynamic stresses are characterized and related to such variables as the imposed velocity, core thickness and its relative density, as well as the strain-rate sensitivity of the material. Comparisons between measurements and simulations are presented in Section 6.

2. Test protocol

All test specimens were fabricated from 304 stainless steel. To produce the test configurations, an array of slotted strips was assembled in a rectangular wine box configuration (Figure 2). The web dimensions were $h = 0.25$ mm and $H = 25$ mm, with slenderness characterized by $H/h = 100$ and relative density $\bar{\rho} = h/L_1 = 0.02$. Once assembled, the core members were attached to top and bottom face sheets (each 1.5 mm thick) by placing small amounts of braze material at the intersection points (a mixture of
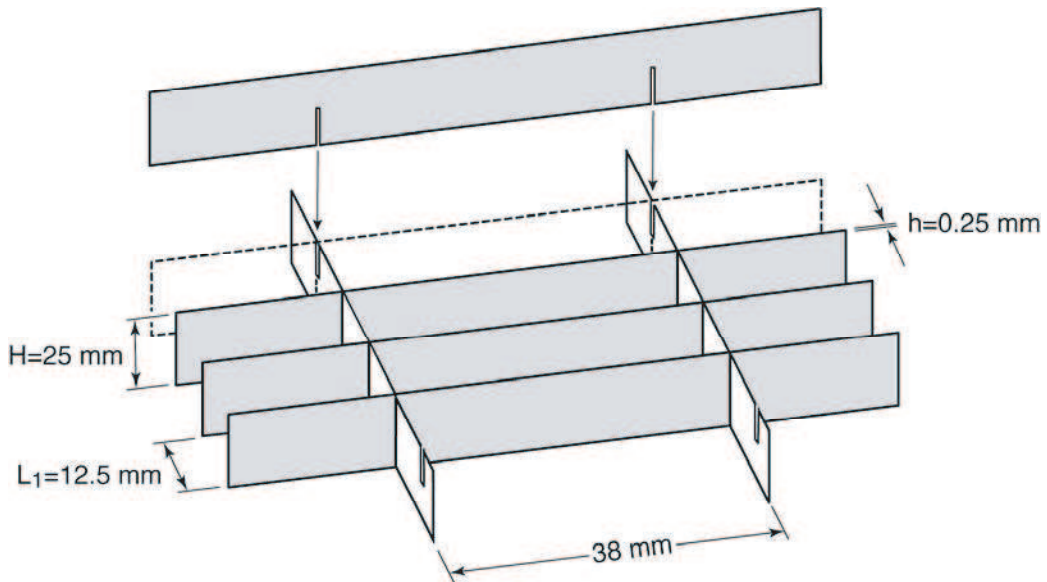

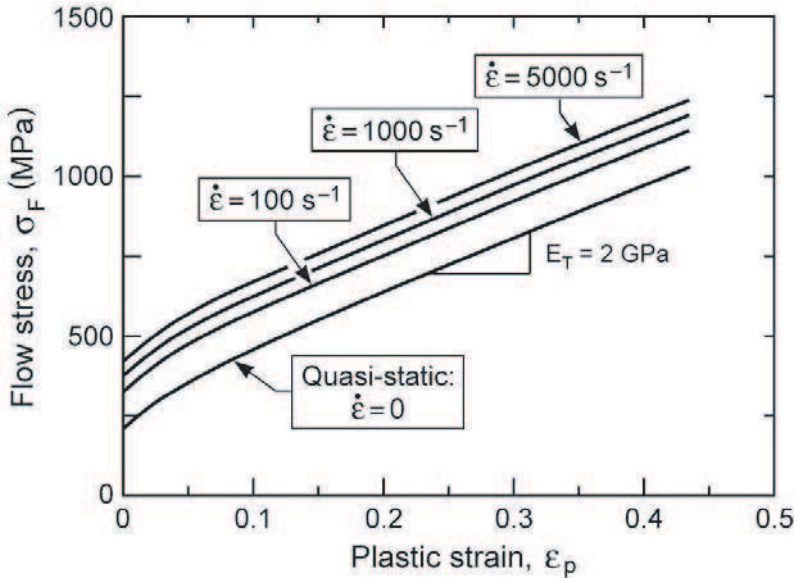**Figure 2.** Schematic of core assembly method and pertinent dimensions.

Figure 3. Quasistatic and dynamic flow characteristics of 304 stainless steel.
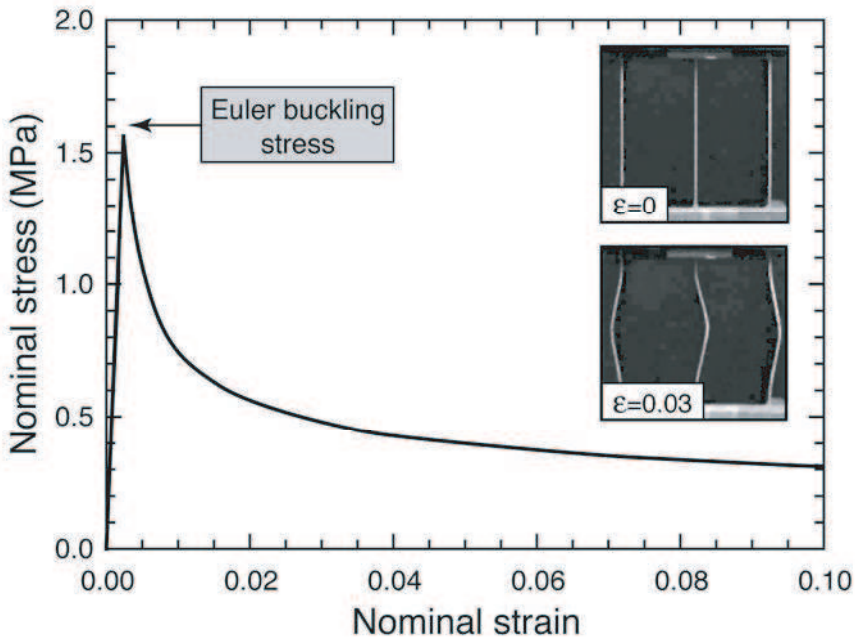

Figure 4. Quasistatic compressive response of I-core specimen.

Nicrobraz Cement 520 and Nicrobraz 31 braze powder, provided by Wal Colmonoy, Madison Heights, MI) and heating the assembly in vacuum for 2 hours at 1075° C. Specimens were cut from the panels using electro-discharge machining. Each was 32 mm square and contained three parallel web members, spaced 12.5 mm apart. Regions containing the transverse, widely spaced, web members were discarded (these members were used solely to provide support to the longitudinal members during assembly and brazing).

Dynamic through-thickness compression tests were performed in a gas gun using cylindrical Al 7075-T6 projectiles 45 mm in diameter and 50 mm long. The test specimens were mounted onto a 2.6 m long Hopkinson bar, instrumented with two 350 strain gauges in a half Wheatstone bridge configuration, positioned at mid-length. The event window was $\sim 500\,\mu s$, dictated by the time required for the incident pulse to reflect off the back surface and return to the gauge location. This duration is significantly greater than that needed for core crushing under the test conditions employed. The impact velocity was measured by three pairs of laser diodes at the end of the gun barrel. It was varied between 75 and 160 m/s. For comparison, quasistatic compression tests were also performed, at a nominal strain rate of $10^{-4}\,s^{-1}$.

Images obtained using a high speed camera (Imacon 200, DRS Technologies) were used for two purposes: (a) the sequences confirmed that the imposed velocity was constant over the relevant time period and consistent with that measured by the laser diodes, and (b) buckling patterns were recorded at periodic time intervals and subsequently used for assessment of the numerical simulations.

The quasistatic and dynamic plastic properties of the alloy were obtained from previous studies [Stout and Follansbee 1986; Xue and Hutchinson 2006; Zok et al. 2005] and are reproduced in Figure 3. The rate sensitivity of the initial yield stress is characterized by

$$k \equiv \sigma_y(\dot{\varepsilon}_p)/\sigma_y^o = 1 + (\dot{\varepsilon}_p/\dot{\varepsilon}_0)^m, \tag{1}$$

where σ_y^o is the quasistatic yield stress (200 MPa), $\dot{\varepsilon}_p$ is the plastic strain-rate, $\dot{\varepsilon}_0 = 4,920\,s^{-1}$ and $m = 0.154$. The rate-independent, quasistatic limit has $\dot{\varepsilon}_P/\dot{\varepsilon}_0 \to 0$, or, equivalently, $k = 1$. The hardening rate is strain rate independent. Additionally, in the domain $\varepsilon_p > 0.05$, the hardening rate is constant, characterized by a tangent modulus $E_T \approx 2\,GPa$.

3. Experimental results

Results from a representative quasistatic compression test (Figure 4) reveal a stress maximum and subsequent rapid softening caused by elastic buckling. The peak value (1.5 MPa) correlates well with that predicted by the Euler buckling formula (assuming clamped ends) and well below the predicted yield stress: $\sigma_Y \bar{\rho} \approx 4\,MPa$. Moreover, the buckling pattern (shown in the inset) is consistent with the shape of the fundamental mode.

In contrast, the dynamic buckling response involves short wavelength buckles, typically an order of magnitude smaller. Two representative sets of images of the buckling sequence are presented in Figure 5. In one case, the specimen is viewed parallel to the plane of the web members; in the other, the viewing direction is at 20° to this plane, thereby revealing the faces. These complementary views show the progression of short wavelength buckles, initiating near the impacted face and propagating as a wave towards the opposite face. For the projectile velocity employed (95 m/s), the time required for this bucklewave to reach the back face is about 30 μs. In the inclined orientation, the images also reveal the
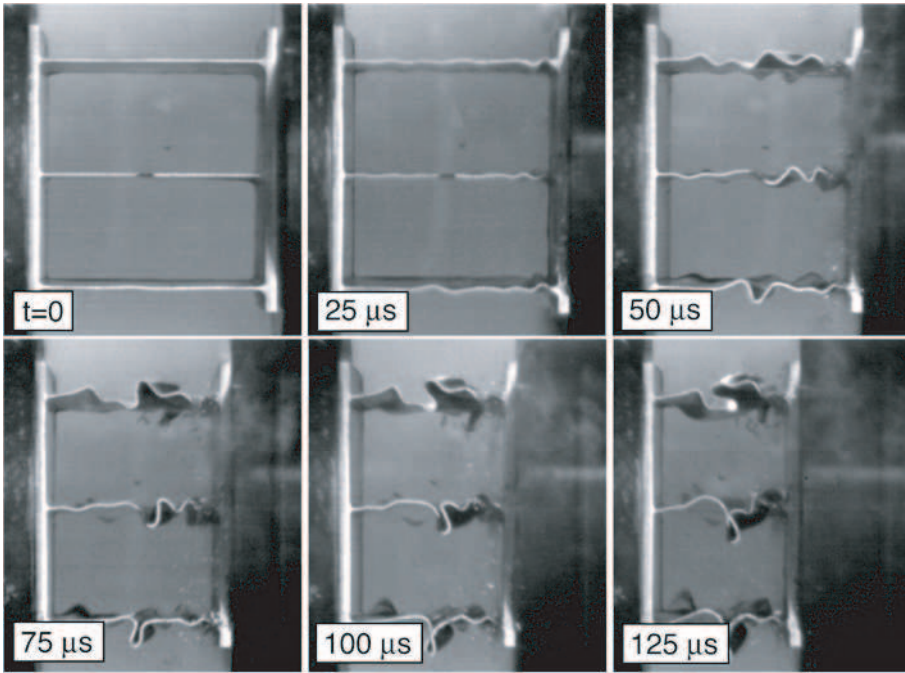
(a)
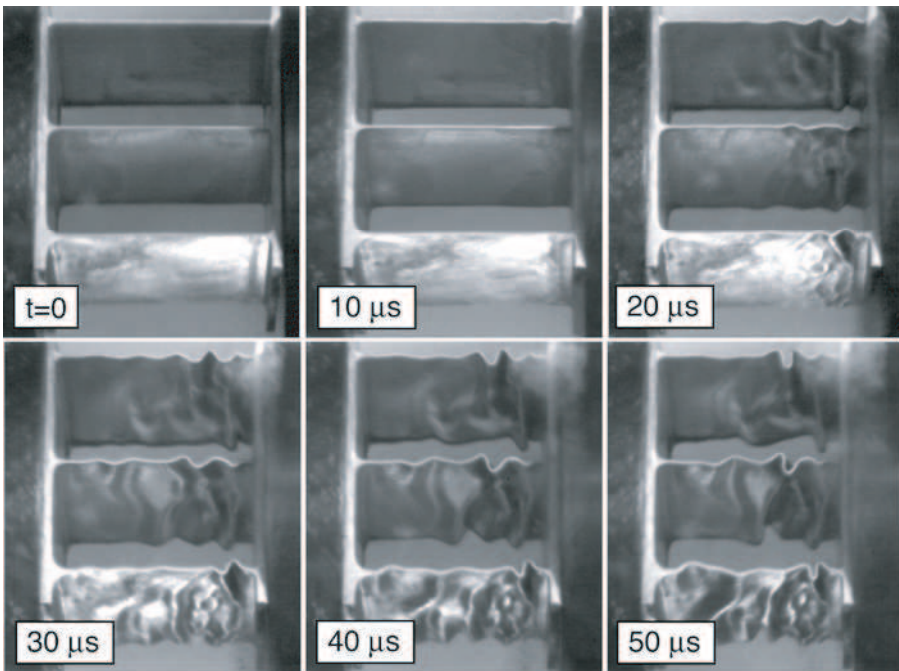
(b)

Figure 5. Buckle wave formation in I-cores at imposed velocity $v_0 = 95$ m/s. Specimens viewed (a) parallel to, and (b) at 20° to the web members. In both sequences, the projectile just makes contact with the right side of the specimen in the first frame (labeled $t = 0$).

presence of transverse buckles, manifested as undulations normal to the direction of imposed velocity. This feature highlights the three-dimensional nature of the bucklewaves and motivates the subsequent numerical investigation.

Additional features of the bucklewaves are gleaned from detailed comparisons of the buckle patterns (when viewed on-edge) at various time intervals. Representative profiles for three web members for an incident velocity of 95 m/s are plotted on Figures 6a—6c. In each case, the buckle pattern at short times exhibits 4—5 peaks. As buckling proceeds, some of the buckles grow more rapidly than others, essentially consuming adjacent buckles of smaller amplitude (examples indicated by open circles). One manifestation of this process is an apparent reduction in bucklewavelength with increasing time. Eventually, at large strains, only one or two buckles survive. These features are also apparent from the crushed samples, which exhibit only one or two dominant folds in each web member. The implications are twofold. First, the bucklewavelength at prescribed velocity is not ordained, but rather evolves with time. Similar features emerge from the numerical simulations presented in the next section as well as from an analytical model for bucklewave evolution [Vaughn and Hutchinson 2006]. Second, postmortem examinations of crushed specimens provide no information on the evolution of buckle patterns, especially
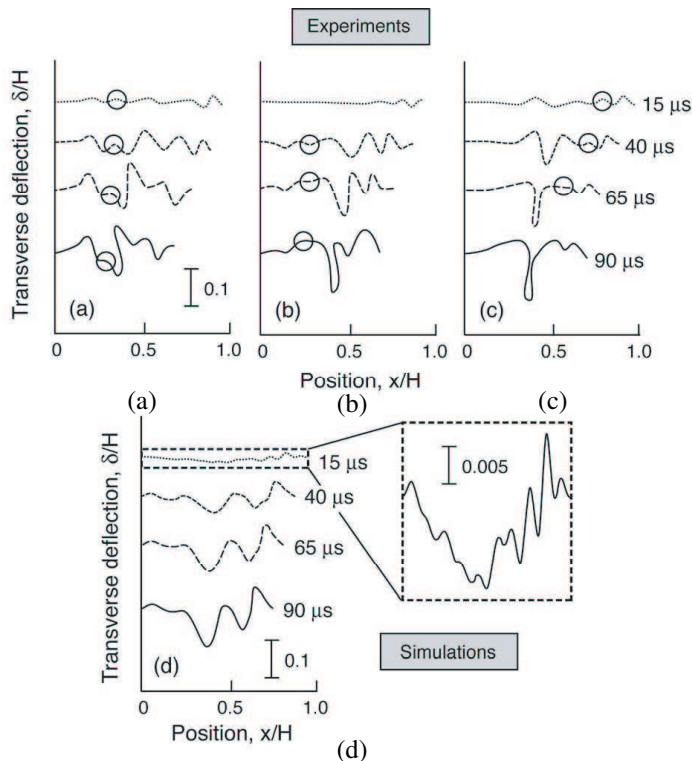

Figure 6. (a)–(c) Buckle patterns obtained from high speed photography at imposed velocity $v_0 = 95$ m/s at several times after impact. The circles show examples of buckles that were well defined in the early stages but were subsequently consumed by the growth of adjacent buckles. (d) Simulations corresponding to experimental measurements. Inset shows detail of the buckle pattern at the earliest time.

those that were present in the early stages of crushing and dominated the loading response. In situ observations are crucial in this regard.

The corresponding back face response is characterized by three stages (Figure 7a): (i) a rapid rise, peak, and decay in stress over a period of about 30 μ s, coincident with the time for bucklewave propagation; (ii) an extended irregular plateau at significantly reduced stress level, accompanying the large scale collapse of the web members; and (iii) a rapid hardening domain as the compressive strain approaches unity, characterized by $v_0 t / H \approx 1$. The initial peak is essentially independent of the imposed velocity (over the range 75–165 m/s), but exceeds the quasistatic stress by a factor of about 5 (Figure 7b). This elevation is attributable to both strain rate sensitivity of the plastic response and inertial stabilization of long wavelength buckles at high velocities [Vaughn et al. 2005; Vaughn and Hutchinson 2006; Wei et al. 2007]. These effects will become apparent in the ensuing numerical assessment.

4. Establishing the buckling modes
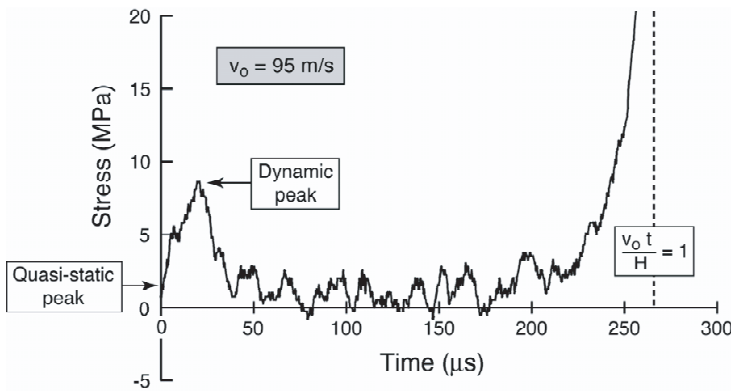
(a)
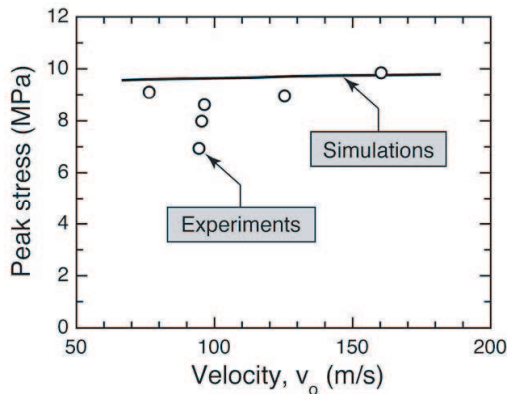
(b)

Figure 7. Dynamic compressive response of I-core specimen.

4.1. *Geometry and boundary conditions.* The geometric variables used in the numerical investigation are depicted in Figure 8. A unit cell is defined with periodic boundary conditions. In most cases the cell is square in plan view, such that $L_1 = L_2 = L$, and has cross sectional shape with fixed ratio of edge length L, to core height H (specified as $H/L = 2$). Most calculations use a slenderness $H/h = 100$, with relative density $\bar{\rho} = h/L \equiv 2h/H = 0.02$. In some instances, the slenderness is varied in the range $50 \le H/h \le 400$ (while retaining the shape $H/L = 2$).

4.2. *Finite element method.* The unit cell has been analyzed by the commercial code, ABAQUS/Explicit. Four-node shell elements (S4R) with five integration points through the thickness are used to model both the faceplates and the core members. Manufacturing imperfections are incorporated into the calculations. Periodic boundary conditions are applied, except at the front and back faces. A uniform velocity boundary condition is imposed on the front. To encompass the responses of interest, the parameter ranges have been selected in accordance with the following four considerations. First, in typical panels subject to water blast, front face velocities up to $v_0 = 100$ m/s are induced [Fleck and Deshpande 2004; Xue and Hutchinson 2004]. Velocities from 10 to 500 m/s capture most of the realistic possibilities. Unless stated otherwise, the results are for 100 m/s. Second, the core thickness, H, is varied between the small values used for the experiments (25 mm) to the large values expected for actual panels (0.3 m). Unless stated otherwise, the thickness is taken to be $H = 0.2$ m. Third, within the slenderness range $50 \le H/h \le 400$, the core relative density is varied over $0.005 \le \bar{\rho} \le 0.04$, thereby spanning the transition from soft to strong responses. Unless stated otherwise, the results are for $H/h = 100 (\bar{\rho} = 0.02)$. Fourth, the responses are somewhat dependent on the strain rate sensitivity of the material. Most results include this sensitivity. In a few cases, where fundamental insights are needed, a strain rate insensitive material has been used.

In most cases, to be as close as possible to the experimental arrangement, the back face is placed on a rigid foundation. This support will cause the responses to differ from those for a free back face, such as the center of a panel subject to blast.

4.3. *Buckling modes.* Before embarking on detailed dynamic calculations, the distribution of imperfections capable of duplicating the experimentally measured buckle patterns over the complete velocity
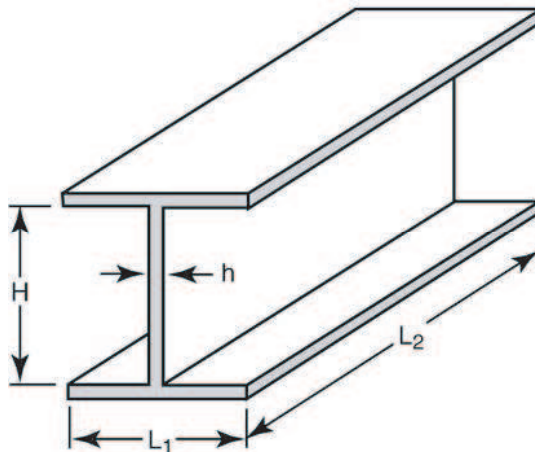

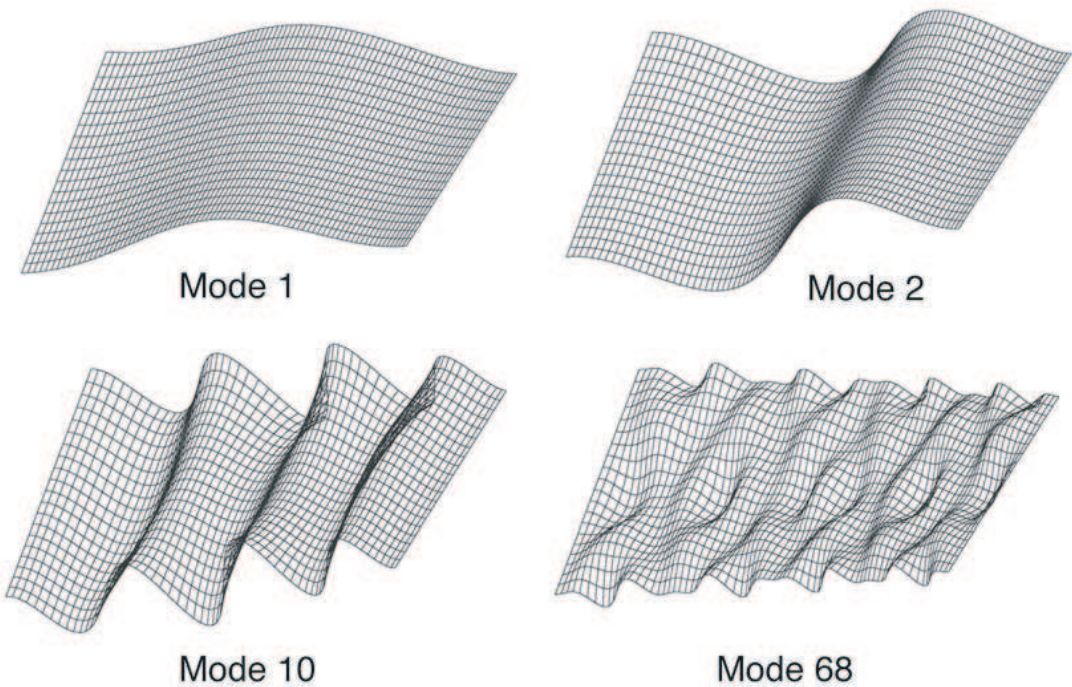**Figure 8.** Cell model used in finite element calculations.

Figure 9. Examples of the buckle patterns calculated for four eigenmodes (1, 2, 10, 68).

range (from quasistatic to the highest velocity, $v_0 = 500$ m/s) must be ascertained, commencing with insight gained from the experimental observations (Figures 4 and 5). The following three steps have been undertaken.

(i) The eigen-modes have been ascertained and those having features similar to the experiments are identified. Four selected modes are summarized on Figure 8. Evidently, among these, mode 68 exhibits buckle patterns most similar to the dynamic bucklewaves, including both axial and lateral wavelengths. This combination of orthogonal wavelengths provides a sufficient number density of imperfections that the dynamic modes are reproduced with acceptable fidelity.

(ii) Dynamic calculations of the stresses transmitted into the back face are performed using various modes, incorporating a range of imperfection amplitudes. The salient results are summarized on Figure 10. Note that all imperfections have a dramatic influence on the stress, so that calculations without imperfections are inadequate. Once imperfections are introduced, thereafter the effects are less pronounced. The perspective taken for this investigation is that, since the amplitudes of imperfections present in actual I-core panels are difficult to specify or measure, a realistic choice is made that gives acceptable agreement with the present experimental observations. Thereafter, the amplitudes are held constant. An independent, more detailed, investigation of the influence of imperfection amplitude will be reported elsewhere.

(iii) To adequately encompass the buckling response over the full velocity range, it is not sufficient to use modes that provide buckle patterns representative of the highest velocities, because these
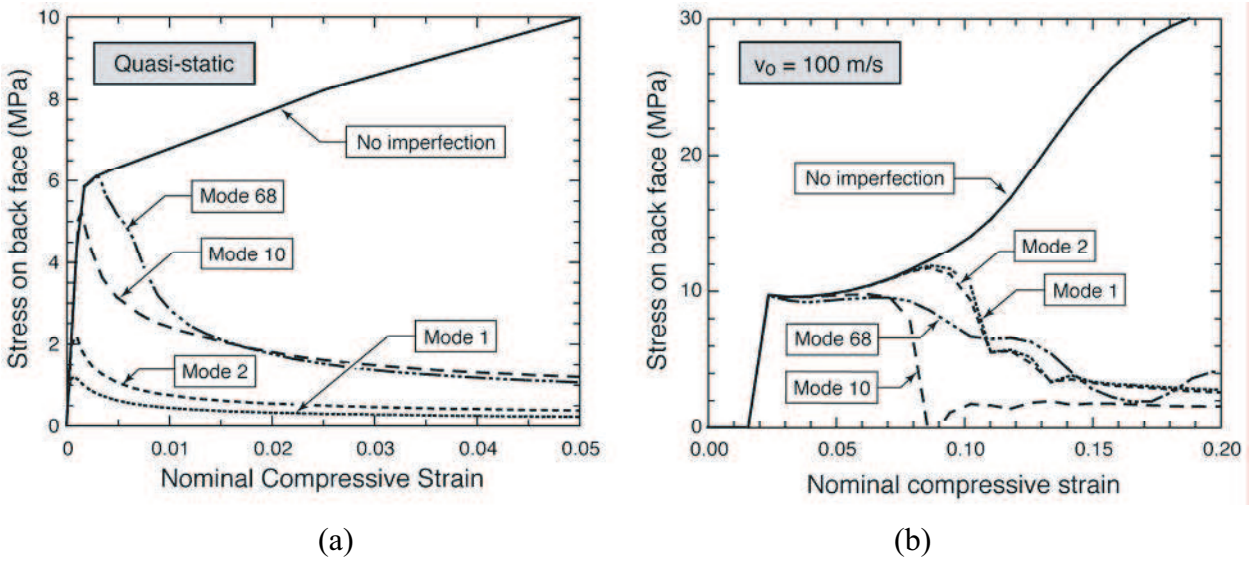
Figure 10. Effects of imperfection mode on (a) quasistatic and (b) dynamic response. (Imperfection amplitude $\xi = 0.15$).

do not reproduce the quasistatic response, and vice versa. For instance, for quasistatic loading (Figure 10a), the mode 1 imperfection yields the lowest buckling stress (at 1.2 MPa comparable to the measurements) and a buckling mode consistent with that observed experimentally. In contrast, under dynamic conditions, to capture the buckle patterns (Figure 9) and peak stresses (Figure 10b), higher modes are required. Consequently, to embrace all possible responses, several representative modes are combined. But, before proceeding, the sensitivity of the buckling response is ascertained, both to the modes selected and the way in which they are combined. The objective is to assure that the calculations have generality and are insensitive to the specific choices. Overall, the results reveal that the most important to include are mode 1 plus one high mode (such as 68). For smooth trends with velocity, two intermediate modes (2 and 10) are also included in subsequent simulations.

To be consistent with the nature of manufacturing imperfections, the amplitude δ corresponding to each mode is taken to be proportional to the respective longitudinal wavelength. For instance, if the amplitude for mode 1 is selected as $\xi \equiv \delta/h = 1$, the amplitude for mode 68 is $\delta/h = 1/7$ (refer to the buckle pattern on Figure 9), and so on. Using this approach, the bucklewavelengths emerging from the calculations at the highest velocity are smaller than those associated with the highest eigen-mode (compare, for example, the buckle pattern at 500 m/s in Figure 11 with the mode 68 imperfection in Figure 9). Visually, these modes appear similar to those found experimentally at comparable velocity (Figures 5 and 7). The ability of ABAQUS to select the short wavelengths is attributed to the through-width variation in buckle shape associated with the highest modes (Figure 9). This variation provides an infinite number of permutations in available wavelength in any direction. These results provide some assurance that the dynamic modes selected are not excessively constrained by the initial imperfections.

In all ensuing calculations, combined imperfections are used. The stress/strain curves used as input are those applicable to 304 stainless steel, plotted on Figure 3 and described by Equation (1). In a few cases,
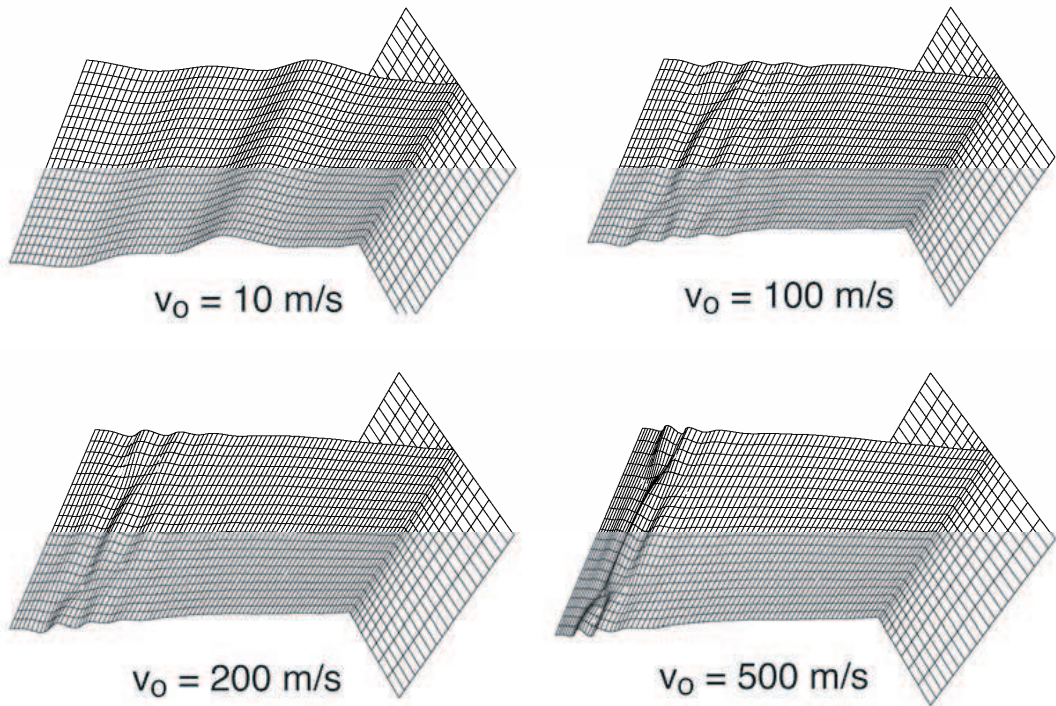
Figure 11. Buckle waves induced at several imposed velocities. Note that the wavelengths at the highest velocities are shorter than those of the initial imperfections (Figure 9). ($H = 25$ mm, $\bar{\rho} = 0.02$).

to gain insight, the strain rate dependence has been excluded. With a Young's modulus $E = 200$ GPa and a mass density $\rho = 7,800$ kg/m^3, the elastic wave speed through this material is $c_{el} = \sqrt{E/\rho} \approx 5,000$ m/s. All calculations are performed by imposing a constant velocity v_0 at one end.

4.4. *Stress wave propagation.* Stress wave propagation down the core members is characterized by performing calculations without imperfections, because the members remain straight (no buckling) up to large strains (Figure 10). The plastic strain distribution at various times after the velocity is imposed is presented in Figure 12 ($H = 25$ mm). Results determined for the rate-independent material (Figure 12a) reveal the propagation of a plastic front with velocity $v_{pl} \approx 800$ m/s and constant strain in the wake. The response is similar to that reported for annealed Cu [Von Karman and Duwez 1950], except that the velocity and plastic strain are higher.

When the elastic wave reaches the back face, at $t = H/c_{el} \approx 5 \, \mu$s, a secondary plastic front with small plastic strain emerges from the back face and advances towards the incident front. Neglecting the short time associated with the transmission of the elastic wave, the time for convergence of the plastic fronts is $t_{pl} \approx H/2v_{pl}$. Convergence of the two waves causes a slight increase in the plastic strain in the wake of the incident front. Significant elevations in plastic strain develop only after the incident plastic front reaches the back face, at $t = H/v_{pl} \approx 40 \, \mu$s. Repeating the calculations with a rate-dependent material (Figure 12b) indicates that the plastic front is now much more diffuse, with a broader distribution of
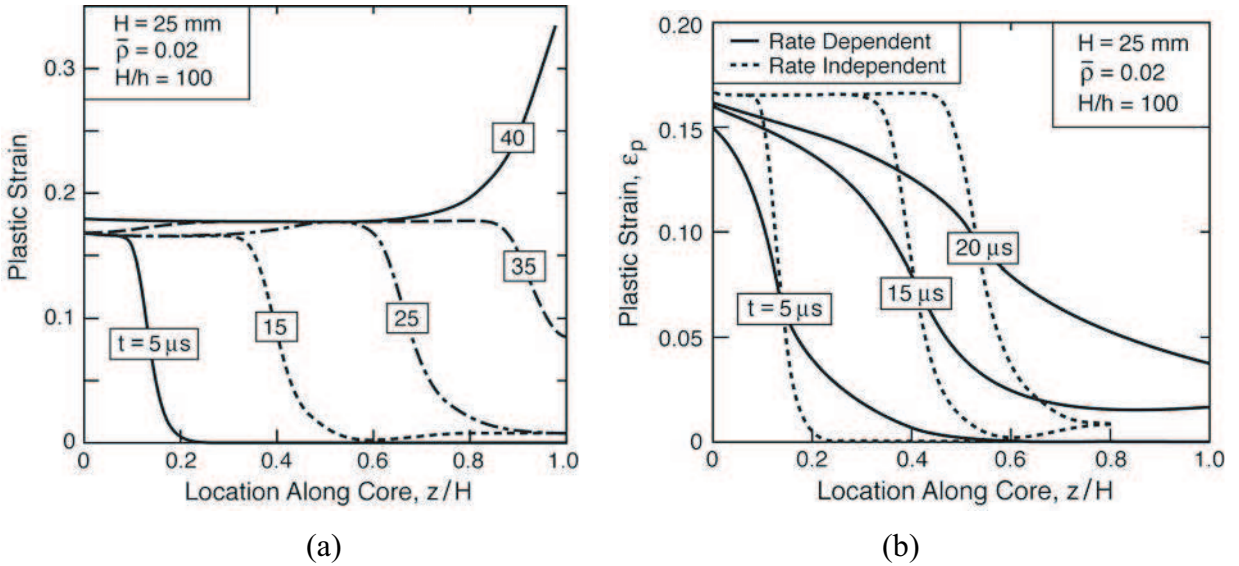
Figure 12. Temporal variation in plastic strain distribution calculated for a core without imperfections (to suppress buckling) subject to velocity $v_0 = 100$ m/s. (a) Rate independent material, and (b) Comparison between rate dependent and rate independent materials.

plastic strain. Moreover, the plastic front propagates more rapidly than in the rate insensitive material. If a plastic strain of 1% is specified to define this front, its velocity is computed to be $v_{pl} \approx 1,800$ m/s. The consequences will become apparent when the stresses are discussed below.

4.5. *Buckle wavelengths.* When imperfections are present, bucklewaves become evident in the wake of the plastic front shortly after the velocity is imposed (Figure 11). Their subsequent evolution, characterized by lateral displacement profiles, is illustrated in Figure 6d for one specific case. In the early stages ($\leq 20\,\mu$s after the velocity is imposed), the profile exhibits about 10 peaks with an average wavelength $L_c/h \approx 10$. Thereafter, the number of peaks diminishes as some peaks are consumed by growth of adjacent ones. For instance, after $100\,\mu$s, only 3 or 4 peaks remain with an average wavelength $L_c/h \approx 20 - 30$.

For comparison, the wavelengths predicted from a free-flight model are calculated [Vaughn and Hutchinson 2006]. The model predicts that L_c scales with the length L_o of a clamped plate at the onset of buckling when compressed quasistatically into the plastic range. Tangent-modulus theory gives L_o as:

$$\frac{L_o}{h} = \pi \sqrt{\frac{E_T}{3\sigma}}. \tag{2}$$

In the present context, σ is taken as the dynamic stress in the plastic region prior to buckling. For a rate-independent material with bilinear stress/strain characteristics, this stress is uniform over the length

and is accurately described by the relation [Vaughn and Hutchinson 2006]:

$$\frac{\sigma}{\sigma_Y \bar{\rho}} \approx 1 + \sqrt{\frac{E_T}{E}} \left(\frac{v_0}{c_{el} \varepsilon_Y} - 1 \right). \tag{3}$$

Upon combining Equations (2) and (3), the critical length becomes:

$$\frac{L_o}{h} = \pi \left\{ \frac{3\sigma_y}{E_T} \left[1 + \sqrt{\frac{E_T}{E}} \left(\frac{v_o}{c_{el} \varepsilon_y} - 1 \right) \right] \right\}^{-1/2}.$$

For $v_o = 100$ m/s, the predicted wavelength is $L_o/h \approx 3$. The corresponding wavelength ascertained from the numerical simulations (Figure 7d) at the same incident velocity is initially $L_o/h \approx 10$, increasing to 30 in the later stages of buckling. The discrepancy between the analytic and numerical results is an indication of the highly nonlinear nature of the problem and the consequent difficulties in obtaining an accurate analytic solution.

5. Dynamic stresses

5.1. General observations. Representative results for the computed stress/time response in the presence of imperfections are plotted in Figure 13. The following general features emerge:

(i) The front face stress achieves a peak σ^f_{max} almost instantaneously and remains at this level for a characteristic pulse time, t_{pulse}, before dropping abruptly to a much lower steady-state plateau (Figure 13a).
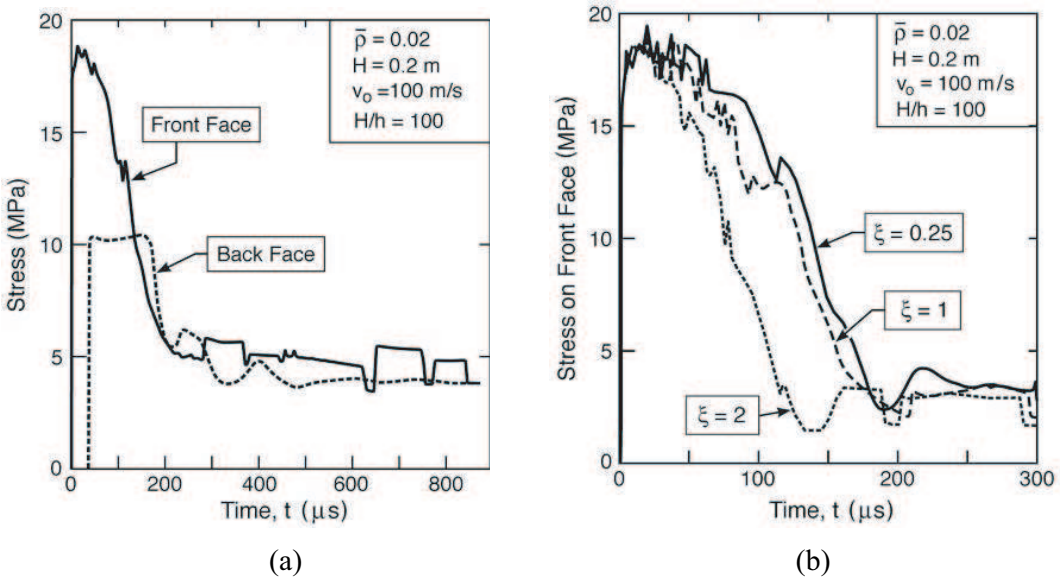

Figure 13. The temporal dependence of the stresses induced on the back and front face when a velocity $v_0 = 100$ m/s is imposed at one end. (Imperfection amplitude $\xi = 1$).

(ii) The back face exhibits similar features, with two notable exceptions. First, the initial plateau stress, σ^b_{max}, is achieved after a short delay, due to the time for transmission of the pressure pulse through the core, given by $t = H/c_{el}$. Second, this plateau is lower than the peak on the front face ($\sigma^b_{max} < \sigma^f_{max}$). Otherwise, the pulse time t_{pulse} and the steady-state plateau stress are comparable on both faces.

(iii) The imperfection magnitude has minimal effect on the peak stresses on both faces. However, t_{pulse} is altered, decreasing as the imperfections become large (Figure 13b).

The governing phenomena and their dependence on core characteristics, material behavior and imposed velocity are elucidated below.

5.2. *Front face stresses.* The maximum front face stress attained at short times, σ^f_{max}, increases linearly with imposed velocity (Figure 14a). Comparisons of σ^f_{max} with the result in (Equation (3)) for a rate-independent material affirms the fidelity of the analytic model (Figure 14b). Upon incorporating strain rate sensitivity, the stress increases, but when normalized by the appropriate σ_Y, at $\dot{\varepsilon} = v_0/H$, Equation (3) retains accuracy adequate for most purposes.

5.3. *Transmitted stresses and pulse duration.* Stresses induced on the back face determined over a wide range of velocity, core thickness, and core member slenderness have the characteristics presented in Figures 15–17. Comparison with and without strain-rate sensitivity (Figure 15) reveals two differences. The rate dependence increases σ^b_{max} by about a factor 2 (from 5 to 10 MPa) and decreases the pulse duration (from 30 to 20 μs). The former is attributed to the strain rate sensitivity while the latter is associated with the more rapid propagation of the plastic front (Figure 12b). Hereafter, to provide a common basis for comparison, the temporal coordinate is normalized by the core height t/H. In some
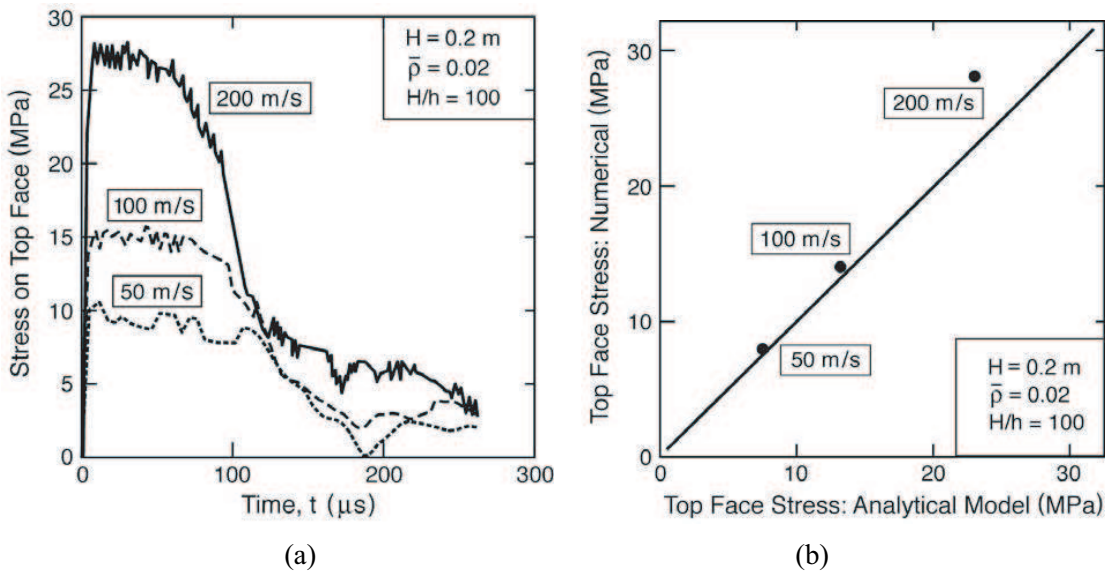

Figure 14. A comparison of the peak front face stress obtained from the numerical simulations with the value estimated from the analytic formula.

plots, the actual stress is used. In others, the stress is normalized: $\sigma / \bar{\rho} \sigma_Y$, where σ_Y is again the yield strength at the nominal strain rate ($\dot{\varepsilon} = v_0 / H$). The key observations are as follows:
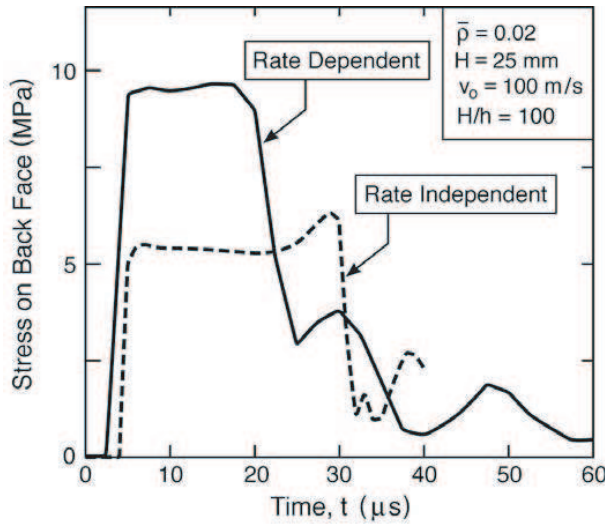

Figure 15. The temporal dependence of the stresses induced on the back face when a velocity $v_0 = 100$ m/s is imposed at one end, including comparison between rate dependent and rate independent materials. Note that the former results in a higher stress but shorter pulse duration.
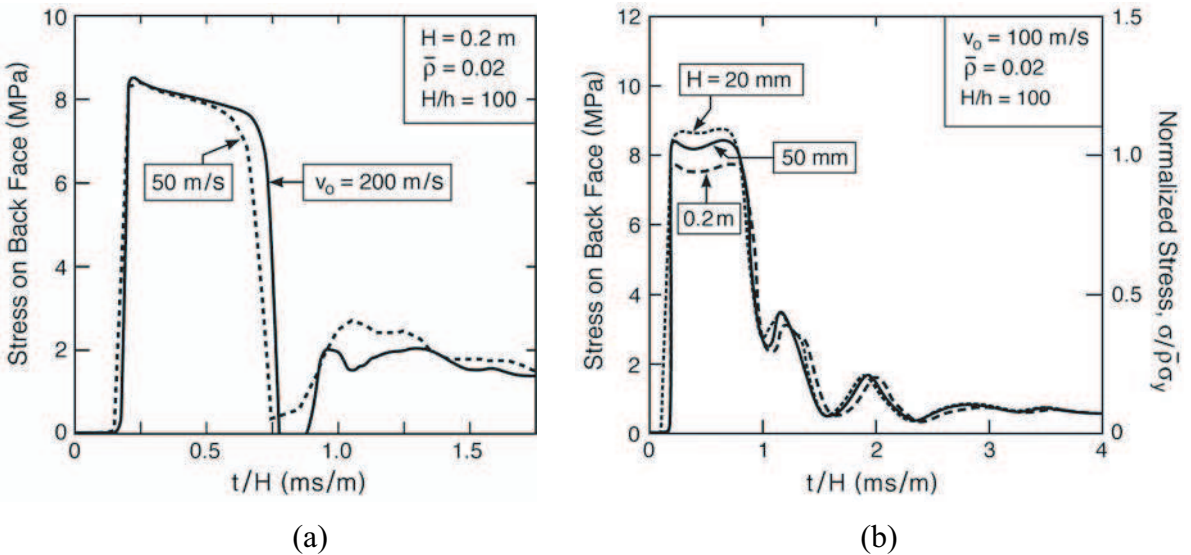

Figure 16. The temporal trends in the stress pulse transmitted through the core, with time coordinate normalized by the core height. (a) Effect of imposed velocity at fixed core height. (b) Effects of core height at fixed velocity.
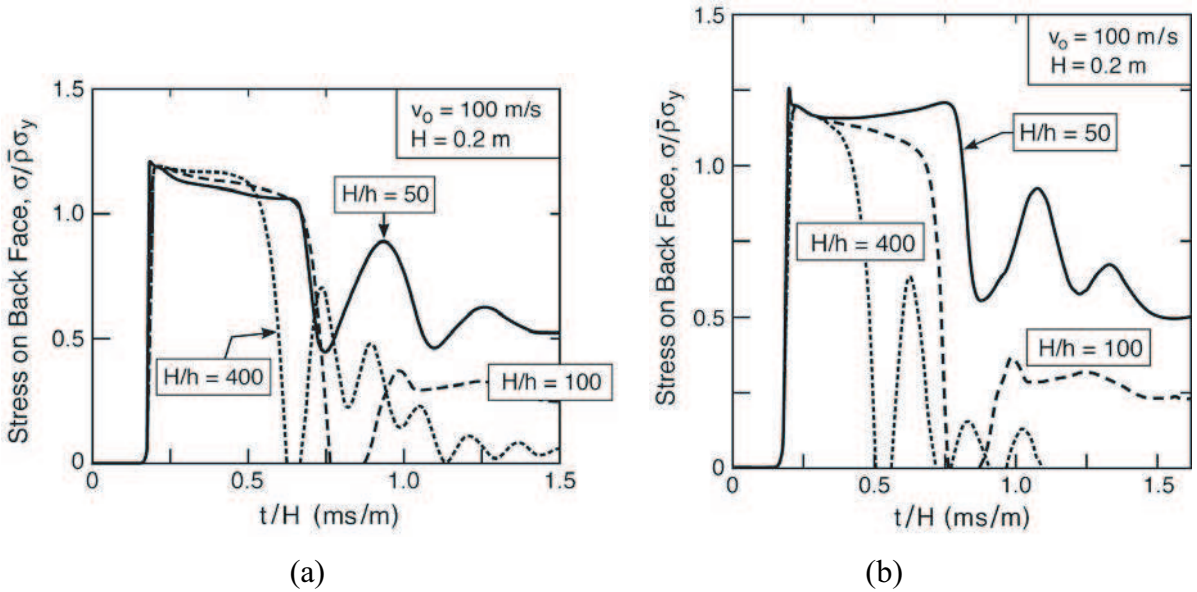
Figure 17. The influence of core member slenderness on the stress pulse transmitted through the core. (a) Imperfection amplitude scaled with the member thickness: $\delta/h = 1$. (b) Constant imperfection amplitude, $\delta = 1$ mm.

(i) For fixed core thickness, the plateau stress and pulse duration are independent of velocity for rate-independent materials (Figure 16a). Moreover, when rate sensitivity is included, the amplitude is larger and the duration shorter (Figure 15).

(ii) Upon varying the core thickness at fixed velocity and slenderness (Figure 16b), the pulse durations become coincident when the time is core thickness normalized. That is, t_{pulse} scales with H. In contrast, σ^b_{max} is almost independent of H.

(iii) The effects of slenderness at fixed velocity and core height depend on the scaling used for the imperfection amplitude. The issues are elucidated by two sets of simulations. One set uses amplitudes that scale linearly with member thickness, $\delta/h = 1$ (Figure 17a), while the other uses amplitudes independent of the slenderness (Figure 17b). In all examples, the normalized peak stress, $\sigma^b_{\text{max}}/\bar{\rho}\sigma_Y$, is unaffected. But there are effects on the pulse duration, t_{pulse}/H. When the imperfection amplitudes are scaled, t_{pulse}/H is almost invariant with slenderness, decreasing slightly for the most slender members. However, when the amplitudes are fixed, t_{pulse}/H decreases systematically with slenderness.

5.4. *Interpretation.* That the pulse duration scales linearly with core thickness indicates a phenomenon dictated by a wave front propagating through the core. To reveal the source, contours of plastic strain are plotted in a time sequence after the imposition of the velocity (Figures 19). These reveal the propagation of a diffuse plastic front from the end exposed to the velocity, as well as the formation of an opposing front
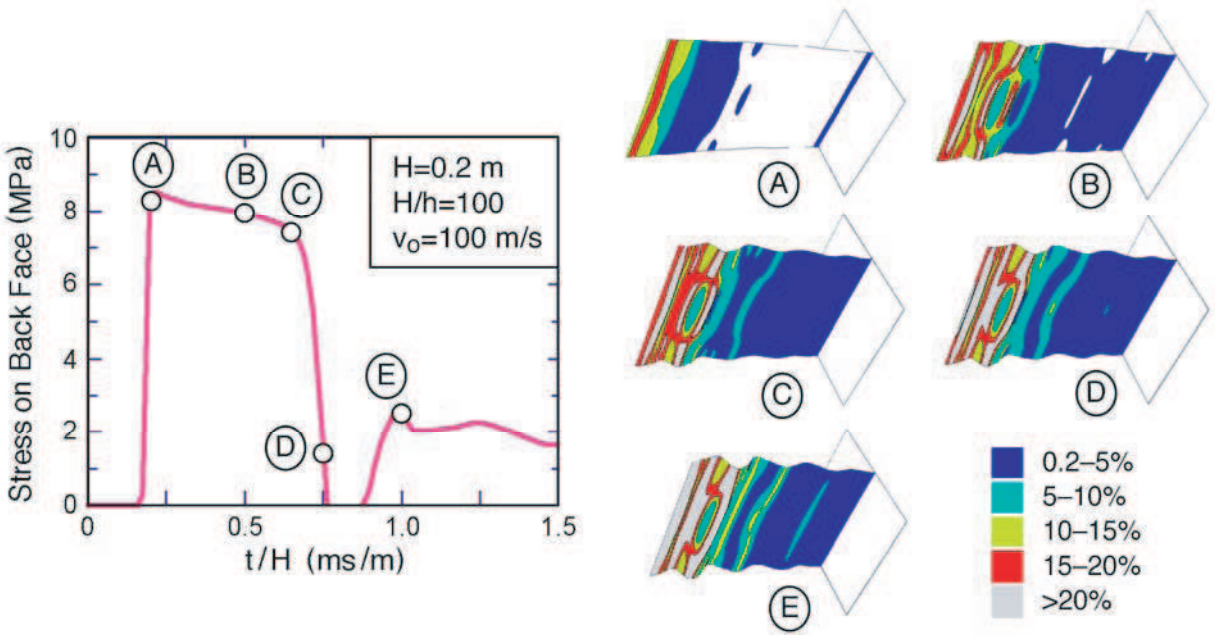
Figure 18. Montage of deformed core members at different times after impact. The colors refer to levels of plastic strain. (Imperfection amplitude: $\xi = 1$).

after the elastic wave reflects from the back face. This is consistent with the behavior obtained for the straight (imperfection-free) core (Figure 12). The bucklewave behind the outgoing plastic front initiates in regions where the strain has exceeded about 10%. These waves propagate at velocity, $v_{bw} \approx v_{pl}$ and reach the back face at time, $t_{bw} = H/v_{bw}$. Inspection of the figures indicates that the stresses remain at the plateau level on both front and back faces, even when bucklewaves are in evidence. That is, buckling near the top face does not immediately cause a reduction in the stresses. Additionally, the pulse terminates approximately at a time when the bucklewave front essentially reaches the back face, at $t \approx t_{bw}$ (Figure 14a). The associated wave velocity is $v_{bw} \approx 800$ m/s for the rate independent material and $v_{bw} \approx 1,200$ m/s for the rate dependent material. These values are consistent with the velocities of the plastic front (Figure 12). They suggest an approximate scaling for pulse duration of the form

$$t_{\text{pulse}} = \lambda(\delta/h) \, H/v_{pl},$$

where $\lambda(\delta/h)$ is a nondimensional parameter of order unity.

In an attempt to provide additional insight into the pulse duration, the evolution of the buckles is monitored by evaluating the spatial variations in the nominal compressive strain along a line parallel to the imposed velocity (Figure 19). The results re-affirm that the buckles become prominent (manifested in large strain undulations) while the stress on the back face is still at its plateau level (see, for example, point A in Figures 18 and 19). However, there is no apparent change in the buckling features at the moment the stress drops from the plateau, between points C and D.
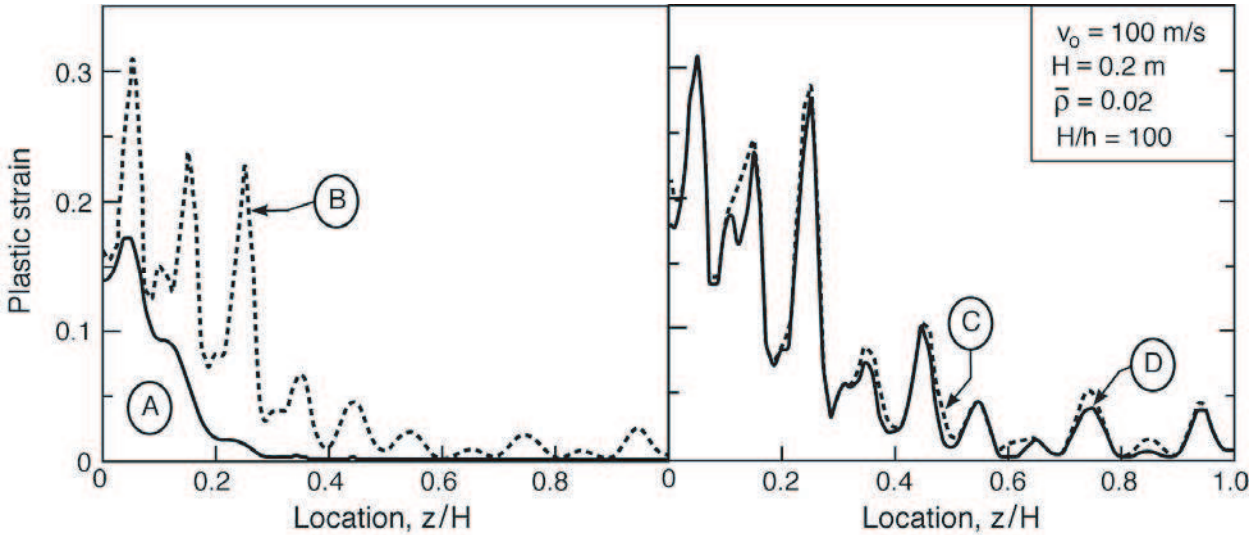
Figure 19. Distribution of plastic strains at various durations after the velocity is imposed. Labels correspond to points in Figure 18.

An understanding of the role of imperfection amplitude and the details of the critical event that triggers the stress drop awaits further numerical investigations. The results of these investigations will be reported elsewhere.

6. Comparison with measurements

An assessment of the numerical results has been made by comparison with the experimental measurements, using the actual test geometries in the simulations. The metrics for this assessment include the peak back face stress, the peak duration and the buckle patterns.

Simulated stress/time curves are presented in Figure 20. Upon comparison with the measurements (Figures 7a), both the peak stress and the pulse duration are captured well, with predicted values of $\sigma^b_{\max} \approx 9 - 10 \, \text{MPa}$ and $t_{\text{pulse}} \approx 30 \, \mu\text{s}$. Moreover, the simulations predict a velocity independent peak in accord with the measurements (Figure 7b). However, a discrepancy exists in the rise time of the initial peak. That is, the simulations predict that the rise should be almost instantaneous (over time $\ll 1 \, \mu\text{s}$) whereas the measured values are typically 10–20 μs. The difference can be attributed to nonuniform loading during the early stages of contact, caused by a small degree of projectile misalignment. For instance, a 1° misalignment at typical velocities would create a 10 μs delay between the point of first contact and that at which contact is complete. Such misalignment is also expected to reduce the peak stresses. Indeed, the measured values fall slightly below the predictions (Figure 7b).

The predicted buckle patterns are compared with the measured ones in Figure 6. When viewed at the same resolution as the measurements, the initial computed profile (at 15 μs) exhibits about 5 peaks: comparable to the measurements. In contrast, when magnified (inset in Figure 6d), the profile exhibits about twice as many peaks. For longer times, the number of peaks diminishes, as some peaks are consumed by growth of adjacent ones. Overall, the predicted buckle evolution is deemed to be a reasonably
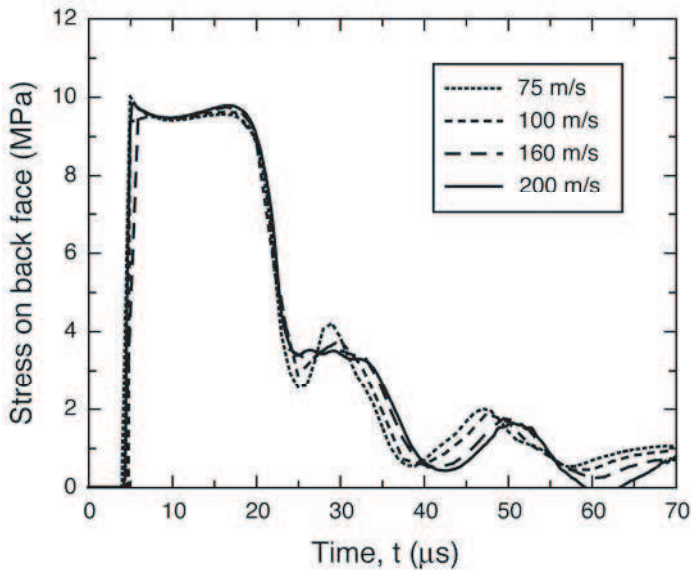
Figure 20. Simulated response of tested I-core specimens ($H = 25$ mm, $h = 0.25$ mm, $\xi = 1$).

accurate representation of that observed experimentally. The inherent variations in the observed patterns (Figures 6a–c) preclude a more rigorous quantitative assessment.

7. Conclusions

Combined measurements and simulations have been used to characterize the response of stainless steel I-core panels supported at the back face and subjected to a constant velocity at the front. Finding a means to incorporate appropriate imperfections has been a major aspect of the assessment. The preferred method combines several prominent buckling modes and assigns imperfection amplitudes proportional to wavelengths. The procedure has been motivated and substantiated by comparing buckle patterns with those found experimentally over the relevant velocity range.

The simulations reveal that the stresses induced differ on the front and back faces. The push-back stress exerted by the core members on the front face are higher and velocity dependent. They are consistent with an analytical formula for straight (nonbuckling) columns. The stresses transmitted through the core to the back face are velocity invariant. They also scale linearly with the product of the relative density and material yield strength. The latter has been substantiated by experimental measurements.

The duration of the stress peak t_{pulse} has been assessed. This duration is essentially the same on both faces, and independent of the incident velocity. Moreover, it scales linearly with the core height H, indicative of a wave propagation phenomenon. Inspection of the numerical results indicates that the pulse terminates when the bucklewave, propagating at velocity v_{bw}, reaches the back face. Accordingly, the pulse time is related to core thickness and bucklewave velocity, such that $t_{\text{pulse}} = H/v_{bw}$. After the pulse terminates, the core continues to compress at a stress level about an order of magnitude smaller.

References

[Abrahamson and Goodier 1966] G. R. Abrahamson and J. N. Goodier, "Dynamic flexural buckling of rods within an axial plastic compression wave", *J. Appl. Mech.* (*Trans. ASME*) **33** (1966), 241–247.

[Fleck and Deshpande 2004] N. A. Fleck and V. Deshpande, "The resistance of clamped sandwich beams to shock loading", *J. Appl. Mech.* (*Trans. ASME*) **71**:3 (2004), 386–401.

[Liang et al. 2007] Y. Liang, A. V. Spuskanyuk, S. E. Flores, D. R. Hayhurst, J. W. Hutchinson, R. M. McMeeking, and A. G. Evans, "The response of metallic sandwich panels to water blast", *J. Appl. Mech.* (*Trans. ASME*) **74**:1 (2007), 81–99.

[Radford et al. 2007] D. D. Radford, G. J. McShane, V. S. Deshpande, and N. A. Fleck, "Dynamic compressive response of stainless steel square-honeycombs", *J. Appl. Mech.* (*Trans. ASME*) (2007). To appear.

[Stout and Follansbee 1986] M. G. Stout and P. S. Follansbee, "Strain rate sensitivity, strain hardening, and yield behavior of 304L stainless steel", *J. Eng. Mater. Technol.* (*Trans. ASME*) **108** (1986), 344–353.

[Tilbrook et al. 2006] M. T. Tilbrook, V. S. Deshpande, and N. A. Fleck, "The impulsive response of sandwich beams: analytical and numerical investigation of regimes of behaviour", *J. Mech. Phys. Solids* **54**:11 (2006), 2242–2280.

[Vaughn and Hutchinson 2006] D. G. Vaughn and J. W. Hutchinson, "Bucklewaves", *Eur. J. Mech. A:Solids* **25**:1 (2006), 1–12.

[Vaughn et al. 2005] D. G. Vaughn, J. M. Canning, and J. W. Hutchinson, "Coupled plastic wave propagation and column buckling", *J. Appl. Mech.* (*Trans. ASME*) **72**:1 (2005), 139–146.

[Von Karman and Duwez 1950] T. Von Karman and P. Duwez, "The propagation of plastic deformation in solids", *J. Appl. Phys.* **21**:10 (1950), 987–994.

[Wei et al. 2007] Z. Wei, M. Y. He, and A. G. Evans, "Application of a dynamic constitutive law to multilayer metallic sandwich panels subject to impulsive loads", *J. Appl. Mech.* (*Trans. ASME*) (2007). To appear.

[Xue and Hutchinson 2004] Z. Xue and J. W. Hutchinson, "A comparative study of impulse-resistant metal sandwich plates", *Int. J. Impact Eng.* **30**:10 (2004), 1283–1305.

[Xue and Hutchinson 2006] Z. Xue and J. W. Hutchinson, "Crush dynamics of square honeycomb sandwich cores", *Int. J. Numer. Methods Eng.* **65**:13 (2006), 2221–2245.

[Zok et al. 2005] F. W. Zok, H. Rathbun, M. He, E. Ferri, C. Mercer, R. M. McMeeking, and A. G. Evans, "Structural performance of metallic sandwich panels with square honeycomb cores", *Philos. Mag.* **85**:26-27 (2005), 3207–3234.

ENRICO FERRI: ef99@engineering.ucsb.edu
Department of Mechanical Engineering, University of California, Santa Barbara, CA 93106-5050, United States

EMILIO ANTINUCCI: emilio@engineering.ucsb.edu
Materials Department, University of California, Santa Barbara, CA 93106-5050, United States

MING Y. HE: ming@engineering.ucsb.edu
Materials Department, University of California, Santa Barbara, CA 93106-5050, United States

JOHN W. HUTCHINSON: hutchinson@husm.harvard.edu
Division of Engineering and Applied Sciences, Harvard University, Cambridge, MA 02138, United States

FRANK W. ZOK: zok@engineering.ucsb.edu
Materials Department, University of California, Santa Barbara, CA 93106-5050, United States

ANTHONY G. EVANS: agevans@engineering.ucsb.edu
Materials Department, University of California, Santa Barbara, CA 93106-5050, United States